Full Article *J. Electron. Mater.*

Structural and thermoelectric properties of nanostructured nominally stoichiometric $Pb_{1-x}Bi_xTe$ prepared by mechanical alloying

Received 00th Month 20xx,
Accepted 00th Month 20xx

DOI: xxx/x0xx00000x

Oliver Falkenbach,[a] Marc O. Loeh,[a] Christoph W. Wiegand[a], Andreas Schmitz[b], David Hartung[c], Guenter Koch[a], Peter J. Klar[c], Eckhard Mueller[a,b,*] and Sabine Schlecht[a]

In this work we investigate the influence of bismuth substituted for lead in lead telluride. The material was nanostructured by mechanical alloying (MA) and was compacted via short term sintering (STS) and, alternatively, hot pressing (HP). Syntheses of samples with substitution up to 6 at.-% of bismuth were carried out twice to ensure reproducibility. All relevant thermoelectric transport parameters were measured in a wide temperature range from 123 K and 173 K, respectively, to 773 K. Two different techniques for measuring the electrical conductivity and the Seebeck coefficient were used, one at low and the other at high temperature. A higher bismuth content of 4 at.-% to 6 at.-% was found to lead to best thermoelectric properties with a maximum *ZT* value of about 0.7 at 723 K for 4.0 at.-% bismuth. The structure was examined in detail via X-ray diffraction (XRD), Raman spectroscopy and transmission electron microscopy (TEM). A key feature of the microstructure is the inhomogeneous distribution of bismuth in the lead telluride matrix and the occurrence of bismuth-rich regions on the nanoscale related to a remarkable increased carrier concentration and mobility.

Keywords: Thermoelectric materials, compacting methods, temperature treatment, Raman spectroscopy.

1. Introduction

A. Basics of thermoelectricity

Thermoelectricity is experimentally mainly represented by two physical phenomena: the Seebeck effect and the Peltier effect. Those effects can be used for converting heat into electricity or cooling a system by driving a thermal flow by applying an electrical current, respectively. Therefore, thermoelectric modules, each containing *p*-type and *n*-type semiconductor materials, can contribute to future energy supply and refrigeration. The conversion efficiency is related to the dimensionless figure of merit $ZT = S^2 \cdot \sigma \cdot T \cdot \kappa^{-1}$ of the material. High efficiency requires high *ZT* and with that a high Seebeck coefficient *S*, high electrical conductivity σ and low thermal conductivity κ at a given absolute temperature *T*.[1] The highest efficiency is found with heavily doped semiconductors, which possess the best combination of these properties.

Lead telluride-based systems have emerged among the most effective thermoelectric materials for applications in the medium temperature range, for example when doped with silver[2], sodium[3] and thallium[4,5], leading to hole-type conduction. Cation substitution

[a] *Institute for Inorganic and Analytical Chemistry, Justus-Liebig-University, Heinrich-Buff-Ring 17, D-35392 Giessen, Germany.*

[b] *Institute of Materials Research, German Aerospace Center (DLR), Linder Hoehe, D-51170 Cologne, Germany. E-Mail: Eckhard.Mueller@dlr.de.*

[c] *Institute of Experimental Physics I, Justus-Liebig-University, Heinrich-Buff-Ring 16, D-35392 Giessen, Germany.*

with aliovalent elements, such as sodium or thallium, results in a rise in the *ZT* value of up to about 1.4 at 723 K due to the generation of resonant states near the Fermi level.[3,4] For the latter case, the performance of the material was found to be independent of the method of synthesis, since ball-milled nanopowders, compacted by hot-pressing, were found to be equal in their thermoelectric performance to ingots from a conventional melting procedure.[5] Nanostructuring offers an alternative way of yielding effective thermoelectric materials. Rare earth-doping using trivalent cerium[6] and yttrium[7] replacing the bivalent lead was also proven effective with a *ZT* value close to 1.

B. The ternary system Pb-Bi-Te

The system $Pb_{1-x}Bi_xTe$ is known to be a thermoelectrically relevant *n*-type material since it was discovered, among others by *Borisova et al.*, that the carrier concentration in lead telluride can be adjusted reliably by appropriate doping with bismuth, which allows one to control the Seebeck coefficient and the electrical conductivity.[8-12] In several studies, *Rogacheva et al.* discussed this ternary system with respect to percolation effects, that were supposed to occur for very low bismuth contents within the solubility limit.[13-15] These effects were found to have an impact on the mechanical as well as the electronic properties. For the bulk, the solubility limit of elemental bismuth in lead telluride, $Bi_x(PbTe)$, is about 1 at.-% to 1.5 at.-%,[13,14] while it increases to about 3 at.-% when adding the compound BiTe thus changing the stoichiometry to $Pb_{1-x}Bi_xTe$.[15] Lately, the process of phonon scattering and its influence on the thermal conductivity were investigated in nanostructured, bismuth-doped lead telluride.[16-19] Nanodots were found in the bulk material.[16] Studies on nanoparticles of lead telluride containing a high fraction of bismuth, synthesized by bottom-up approaches via a micro-emulsion and a direct precipitation technique and compacted via spark plasma sintering (SPS), proved that nanostructuring can help to increase the thermoelectric figure of merit by reducing the thermal conductivity.[17] Another synthetic approach for nanostructured bulk that has already been applied to bismuth-doped lead telluride is an encapsulation technique with small bismuth precipitations embedded in the lead telluride matrix. These reduce thermal conductivity.[18,19]

Combining the concept of nanostructuring with the special effects in the electronic structure of the bulk material discovered earlier we already showed in our previous work on $Bi_x(PbTe)$, that bismuth-doping of lead telluride and nanostructuring via a top-down method in a ball mill, followed by cold pressing plus annealing or hot pressing, yields promising thermoelectric properties.[20] We were able to double the *ZT* value compared to bulk material that was synthesized by matrix encapsulation.

Here we extent the previous work further by studying $(PbTe)_{1-x}(BiTe)_x$, i. e. nominally a $Pb_{1-x}Bi_xTe$ alloy, instead of $Bi_x(PbTe)$, i. e. lead telluride with an excess of bismuth. Furthermore, we used different synthesis and compacting methods. However, as in our previous work we focus on the determination of thermoelectric properties, the underlying structure-property relationship and the reproducibility of these results.

2. Experimental

In the field of developing and characterizing thermoelectric materials, reproducibility of sample preparation and of measurement conditions is always an important issue. In order to address this problem, two series of nominally stoichiometric

bismuth-substituted lead telluride in the range of 1.0 at.-% to 6.0 at.-% (Series A + B) were prepared by using the same nanopowder synthesis and the same compacting method (short term sintering). Furthermore, synthesized nanopowders of the same batch (Series B) were compacted by two different compacting methods, i. e. short term sintering and hot pressing to study the effect of the compacting method on the thermoelectric properties.

A. Syntheses

All nanopowders were synthesized via mechanical alloying (MA) by milling polycrystalline powders of lead (99.9%, -200 mesh, *Alfa Aesar*), tellurium (99.999%, -18 to +60 mesh, *Alfa Aesar*) and bismuth (99.5%, -200 mesh, *Roth*) at a stoichiometry replacing the lead by equimolar amounts of bismuth. 2 g of the powder mixture were milled at a ball-to-powder ratio of 8:1 in a *Retsch* "PM 100" planetary ball mill for 5 h at 450 rpm under argon atmosphere. The reaction was performed in a stainless steel milling beaker (series A: 12 mL, series B: 25 mL) with four stainless steel balls (each 4 g in weight and 10 mm in diameter).

B. Compacting conditions

To study the influence of the compacting method, two different procedures were applied: short term sintering (for Series A + B) and hot pressing (only for Series B).

Short term sintering

Short term sintering (STS) is a technique similar to spark plasma sintering, but using continuous instead of pulsed direct current for heating. The process was performed in a direct sinter press "DSP 510 SE" of *Dr. Fritsch Sondermaschinen*. In all cases between about 0.9 g and 1.2 g of the as-prepared nanopowders were uniaxially compacted. A pressure of 25 MPa was applied and the sample was heated up to 673 K within 6 min while increasing the pressure up to 56 MPa. The temperature was held for 11 min while after 6 min of sintering the pressure was decreased again down to 25 MPa. The samples were cooled down passively at zero load during about 1 h. Pellets with a diameter of 12.7 mm and a thickness of about 1.0 mm were obtained.

Hot pressing

For hot pressing (HP) about 0.9 g of the milled nanopowders were uniaxially compacted at a maximum heating mantle temperature of 523 K. A pressure of 434 MPa was applied for 12 min. The obtained pellets with a diameter of 12.0 mm had a thickness of about 1.0 mm.

C. Characterization methods and measurement parameters

First, the thermal diffusivity α was measured under vacuum via the xenon flash technique using a *LINSEIS* "XFA 500" instrument.

The density ρ of the pellets was determined by the Archimedes method. For calculating the relative density of the samples, a lead telluride bulk density of ρ = 8.16 g·cm^{-3} was assumed.[21] The bulk density of bismuth of ρ = 9.747 g·cm^{-3} was considered according to the corresponding doping level.[21]

The specific heat c_p of bulk lead telluride was taken from the literature as a temperature dependent function of $c_p(T)$ = (48.13 + 9.83·10^{-3}·T·K^{-1}) J·mol^{-1}·K^{-1}.[22]

The thermal conductivity κ was calculated via the equation $\kappa = \alpha \cdot \rho \cdot c_p$. The influence of bismuth on the specific heat capacity was neglected due to the small amount. The uncertainty for all parameters that need to be determined for calculating the thermal conductivity sums up to about 10%.

Low temperature measurements of the electrical conductivity σ were performed using an *Oxford Instruments* superconducting magnet system with magnetic fields up to 10 T. The instrument was cooled by liquid helium. For measuring the electrical resistivity ρ and the Hall coefficient R_H in van der Pauw geometry, four copper wires were used as electrodes soldered via indium contacts onto the sample. The carrier concentration n was calculated using the equation $n = R_H^{-1} \cdot e^{-1}$ with the elementary charge of the electron e. The carrier mobility μ was calculated via the equation $\mu = R_H \cdot \rho^{-1} = R_H \cdot \sigma$. Thus, only one band of carriers was assumed in the analysis of the transport data.

The low temperature Seebeck coefficient S was measured under vacuum with a setup described elsewhere.[23] The system was cooled with a liquid-nitrogen cold finger. Two type E (chromel/constantan) thermocouples were soldered onto the sample by an indium solder for determining the temperature gradient and measuring Seebeck voltages.

The electrical conductivity as well as the Seebeck coefficient above room temperature were measured simultaneously under helium atmosphere at a pressure of 1.1 bar (at room temperature) in a *LINSEIS* "LSR-3 Seebeck" instrument. Platinum electrodes were used for measuring the electrical resistivity. A type S (platinum/platinum-rhodium) thermocouple (for Series A) or a type K (chromel/alumel) thermocouple (for Series B), respectively, were used for measuring the Seebeck voltages. The electrodes were mechanically pressed onto the sample surface. The principle of the electrical conductivity measurement is based on the four-point method. The measurement error can be given as about 5% due to geometrical positioning uncertainty. Regarding the manner of contacting and the differences in the two measurement techniques for both Seebeck coefficient and electrical conductivity, the direct soldering measurements below room temperature can be expected to be more precise.

The temperature cycles for property measurement were done in the following order: thermal diffusivity, high temperature Seebeck coefficient and electrical conductivity (simultaneously), low temperature Seebeck coefficient and electrical conductivity.

For structural characterization, the short term sintered pellets were reground into fine powders. The crystal structure of the products was verified by powder X-ray diffraction (XRD) using a *STOE* "Transmission Diffractometer System StadiP" with monochromatic Cu $K_{\alpha1}$ radiation (λ = 1.5406 Å, monochromator: Ge) at an operating voltage of 40 kV and a current of 40 mA. The powders were measured in quartz capillaries in transmission mode.

Raman spectra were acquired using a *Renishaw* inVia microscope system with a HeNe laser for excitation (λ = 633 nm). The laser was focused with a 50× objective onto the sample surface. The same objective was used to collect the scattered light, which was then dispersed by a spectrometer with a focal length of 250 mm and detected by a CCD-sensor. The system's spectral resolution is limited to 1.5 cm^{-1}. The investigations were carried out in two spectral regions, i. e. from 130 to 1100 cm^{-1} and from 20 to 130 cm^{-1}, respectively. A standard edge filter was used to suppress the Rayleigh scattered laser light in the long wavenumber region whereas a NExT stage had to be used in the short wavenumber region.

Transmission electron microscopy (TEM) including energy-dispersive X-ray emission spectroscopy (EDX) was conducted on a

Philips "CM30" transmission electron microscope equipped with a LaB_6 cathode working at an operating voltage of 300 kV.

Results and discussion

A. Thermoelectric properties

Thermal conductivity

Both compacting methods deliver a relative density of at least 90% for most of the samples, in some cases it is even close to the theoretical bulk density (Tab. I).

Table I. Density of bismuth-substituted lead telluride samples.

Bismuth content / at.-%, Compacting method, Series	Absolute density / g·cm^{-3}), Relative density / %
2.0, STS, Series B	7.336, 90
4.0, STS, Series B	7.634, 93
5.0, STS, Series B	7.387, 90
5.0, HP, Series B	8.164, 99
6.0, STS, Series A	7.411, 90

Comparing to the thermal conductivity of bulk lead telluride[21,24], nanostructuring and alloying with the formal compound BiTe leads to a noticeable decrease of about 50%, depending on preparation and substitution level of individual samples. A rough tendency of a lower thermal conductivity for samples with a higher amount of bismuth can be presumed. The thermal conductivity decreases with increasing temperature due to increased phonon scattering which restricts the thermal transport at higher temperatures. Very low thermal conductivity between 0.4 W·m^{-1}·K^{-1} and 0.6 W·m^{-1}·K^{-1} at 773 K was observed (Fig. 1). The unusual kink at 573 K is an indication of a possible precipitation of nanostructures during the first thermal cycle after compaction which reduces the thermal conductivity further.

The thermal conductivity was found to be the parameter which is most difficult to determine due to microstructural and density fluctuations in the samples and the uncertainty of the xenon flash technique applied for thermal conductivity measurement. The laser flash needs to be newly adjusted for each specimen, thus the conditions are hard to reproduce leading to a larger uncertainty. Structural fluctuations result from the individual preparation procedure with differences in temperature and pressure, especially for the hot pressed sample compared to the others, which can lead to variations in the microstructure different in size and shape during relaxation. These effects partly overlay the influence of slightly different alloying levels. In a first approximation, a linear dependence of porosity on the sample density and thus of the thermal conductivity on the sample density can be assumed.[25]

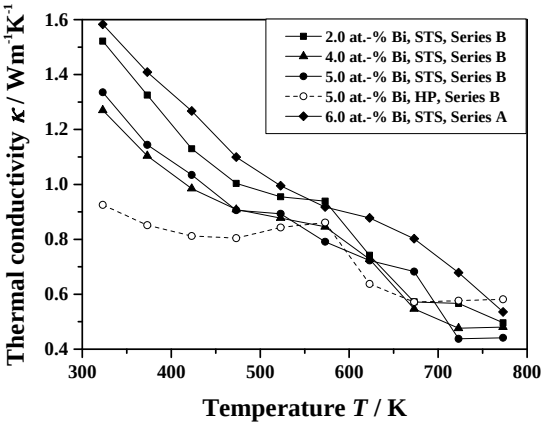

Fig. 1. Thermal conductivity of bismuth-substituted lead telluride samples (first temperature cycle; uncertainty: 10%).

Electrical conductivity

All the other thermoelectric measurements, including electrical conductivity, were carried out after the thermal conductivity measurement.

The formal incorporation of Bi^{3+} on the Pb^{2+} site in the lattice provides additional electrons in the conduction band. This leads to an increasing electrical conductivity with increasing doping rate. For samples with a bismuth content of up to about 3.0 at.-%, the electrical conductivity increases slightly with increasing temperature between 200 K and 450 K. Starting at around 4.0 at.-% to 4.5 at.-% of bismuth, the behavior switches to a semimetallic behavior with an electrical conductivity decreasing towards higher temperatures throughout the whole temperature range investigated here. The same behavior in the electrical conductivity was observed before in nanostructured, bismuth-doped lead telluride.[20] Samples with at least 5.0 at.-% bismuth show high values of the electrical conductivity up to about 1000 $S \cdot cm^{-1}$ at low temperatures (Figs. 2 – 5). One of the highest values in electrical conductivity was observed for a short term sintered sample containing 5.5 at.-% bismuth with about 150 $S \cdot cm^{-1}$ at elevated temperature (Fig. 3). Although a strong temperature-dependence of the band structure (convergence of two crossing valence bands) is well known in lead telluride, we can exclude this single effect here, since it is only effective for *p*-type doping.[26] Thus, there must be another reason for the change of slope in the electrical conductivity in the medium temperature range that shifts over temperature with variation of bismuth content. It could be conceivable that nanometer-sized precipitations or clusters of elemental bismuth lead to a higher metallic contribution to the electrical conductivity.[27]

The discontinuity at room temperature that occurs for many of the samples can be attributed to the geometry factor which was considered in the low temperature measurement, but neglected for the other technique. Hence the low temperature measurement delivers more accurate and precise results. It should also be mentioned that the sample density differs and micro-cracks and porosity have an influence on the electrical conductivity. Nevertheless, Fig. 5 reveals that there is no major difference in electrical conductivity between the two sample series. Thus, it is not substantially affected by differences between the compacting methods involved here.

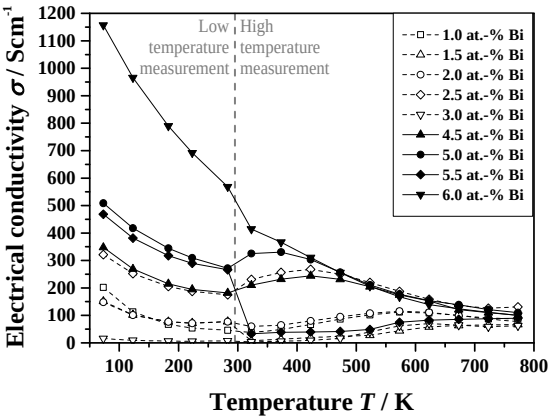

Fig. 2. Electrical conductivity of short term sintered bismuth-substituted lead telluride samples (Series A; uncertainty: 5%).

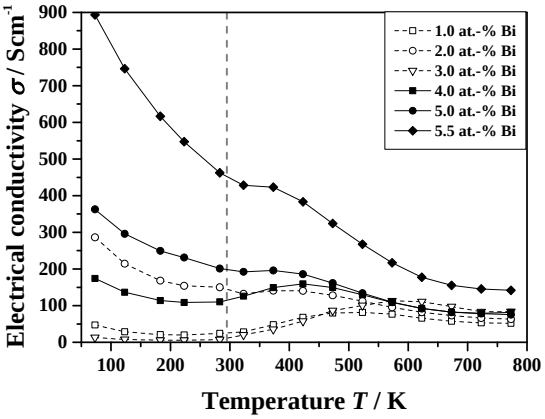

Fig. 3. Electrical conductivity of short term sintered bismuth-substituted lead telluride samples (Series B; uncertainty: 5%).

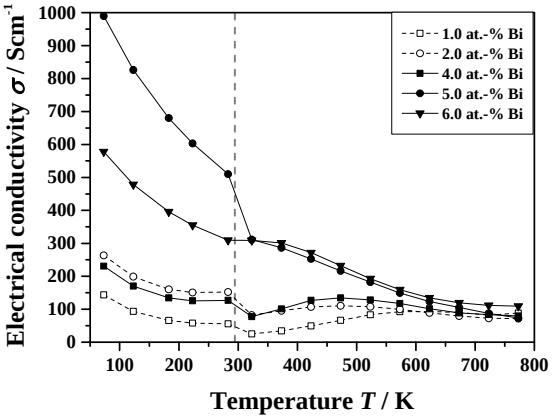

Fig. 4. Electrical conductivity of hot pressed bismuth-substituted lead telluride samples (Series B; uncertainty: 5%).

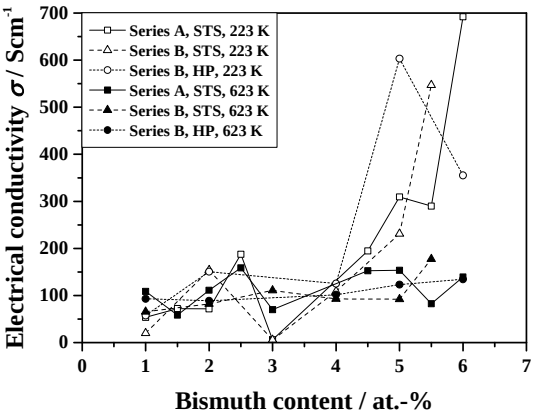

Fig. 5. Electrical conductivity of bismuth-substituted lead telluride samples at 223 K and 623 K, respectively (uncertainty: 5%).

Carrier concentration and carrier mobility

Carrier concentration and mobility near room temperature were determined by jointly evaluating Hall measurements and low temperature electrical conductivity measurements.

Carrier concentration values in the order of 10^{19} cm^{-3} were found (Fig. 6). This is close to the values observed for nanostructured, bismuth-doped lead telluride earlier.[20]

The rapid rise of the electrical conductivity for samples with higher amount of bismuth at lower temperatures can be directly attributed to the increase in the carrier concentration and mobility starting at 3.0 at.-% bismuth (Fig. 6, 7). It can be assumed that for higher bismuth contents the formation of larger, bismuth-rich clusters is favored and also contributes to the behavior observed.[27] The trend in the carrier concentration is in good agreement with previous results on nanostructured, bismuth-doped lead telluride.[20] Opening of a percolation path in the lead telluride matrix when the bismuth content is high enough to cause cooperative behavior in the electronic band structure should result in an even more drastic increase in electrical conductivity and a sharper drop in the Seebeck coefficient caused by a sharp increase in effective carrier concentration and mobility, therefore it is less likely.

The carrier concentrations of nanostructured, bismuth-doped lead telluride are close to those of bulk material with the same amount of bismuth-doping.[8-15] The carrier concentrations found are higher than the ones of thin films.[28-30] This shows that top-down nanostructuring plays an important role in this context. All Hall measurements show negative sign, which is in accordance with the observed negative Seebeck coefficient and proves that electrons are indeed the majority carriers.

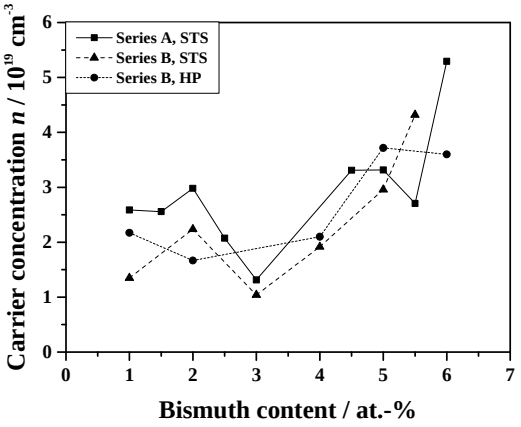

Fig. 6. Carrier concentration of bismuth-substituted lead telluride samples at 280 K (uncertainty: 5%).

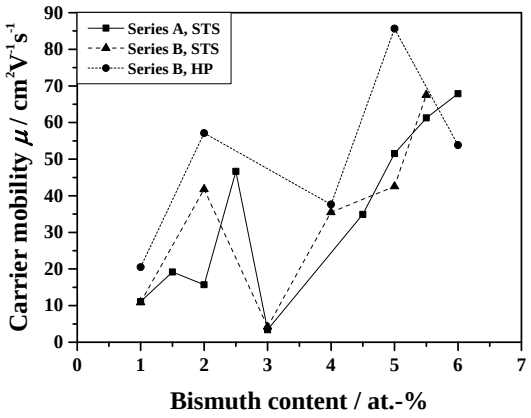

Fig. 7. Carrier mobility of bismuth-substituted lead telluride samples at 280 K (uncertainty: 5%).

Seebeck coefficient

As well known for bismuth-containing lead telluride, all samples show *n*-type conduction over the entire temperature range due to the electron excess coming from the bismuth.[8-15,17,19,20,28-30] The absolute value of the Seebeck coefficient increases linearly with increasing temperature up to a maximum of almost 300 $\mu V \cdot K^{-1}$ at 723 K for 1.0 at.-% bismuth content (Figs. 8 – 11). In accordance with the trend in electrical conductivity, the Seebeck coefficient decreases with increasing amount of bismuth, leading to a reduction of the maximum to only about 200 $\mu V \cdot K^{-1}$ at 723 K for 5.0 at.-% to 6.0 at.-% bismuth-containing samples.

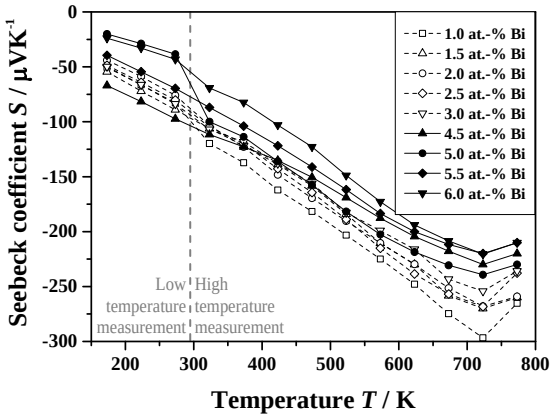

Fig. 8. Seebeck coefficient of short term sintered bismuth-substituted lead telluride samples (Series A; uncertainty: 5%).

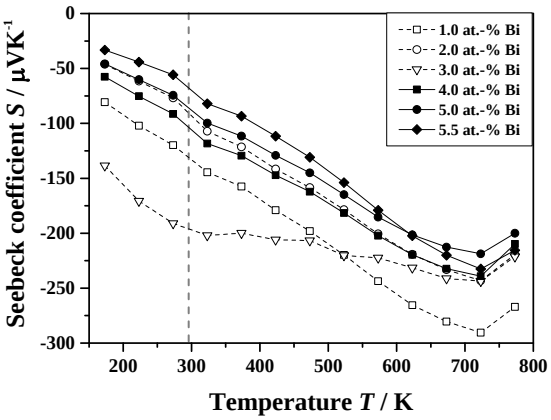

Fig. 9. Seebeck coefficient of short term sintered bismuth-substituted lead telluride samples (Series B; uncertainty: 5%).

An unusual behavior in the Seebeck coefficient is observed at room temperature for a 3.0 at.-% bismuth-substituted sample. The Seebeck coefficient in this sample is higher than in all the other samples (Fig. 9). This is found to be in accordance with a significant drop in carrier concentration and mobility (Figs. 6, 7) and may be a hint to microstructural changes, such as a superstructure, which eventually could occur at this particular bismuth content.

Both the low and high temperature measurement techniques show a high conformity near room temperature since the measurement principle of this parameter is based on zero-current conditions and does not depend on sample geometry or micro-porosity, unlike the electrical and thermal conductivity measurements.

Again, as for the electrical conductivity, no significant dependence on the preparation process was detected. The results of the different sample series were found to be

reproducible and very close to the ones of nanostructured, bismuth-doped lead telluride reported before.[20]

Fig. 10. Seebeck coefficient of hot pressed bismuth-substituted lead telluride samples (Series B; uncertainty: 5%).

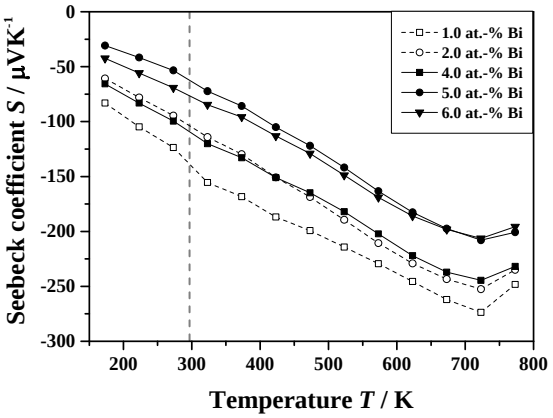

Fig. 11. Seebeck coefficient of bismuth-substituted lead telluride samples at 223 K and 623 K, respectively (uncertainty: 5%).

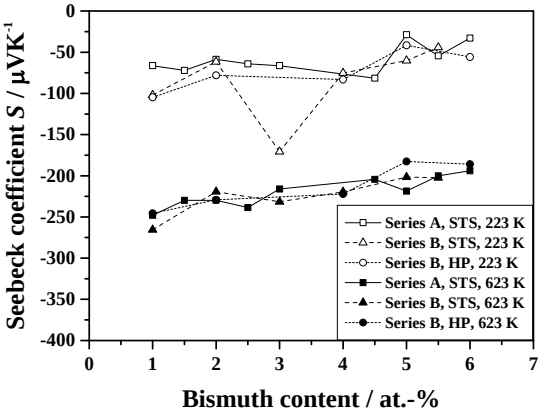

Figure of merit

For the majority of the samples, *ZT* values between 0.5 and 0.7 around 723 K were calculated from the measured data (Fig. 12). A vague trend indicates that samples with higher amount of bismuth are slightly favored, for example a short term sintered 4.0 at.-% bismuth-substituted sample reaches a *ZT* value of 0.7 at 723 K. This result is mainly based on the highest electrical conductivity among all samples together with very low thermal conductivity. The maximum *ZT* value is in agreement with previous work and close to the ones obtained for nanostructured, bismuth-doped lead telluride with similar alloying range and related preparation procedure.[20]

Some uncertainty in the *ZT* is arising from the fact that the thermal conductivity was measured in a first temperature cycle after sample preparation where the nanostructure was changing, most likely by formation of bismuth-rich precipitates. During this process, thermal conductivity was lowering. Accordingly, very low values at high temperature represent a status close to the final stabilized state whereas the values at lower temperatures refer to an intermediate state and are higher than the final ones. Thus, the calculated *ZT* values are somewhat smaller than real at lower temperature, but close to real at highest measured temperature.

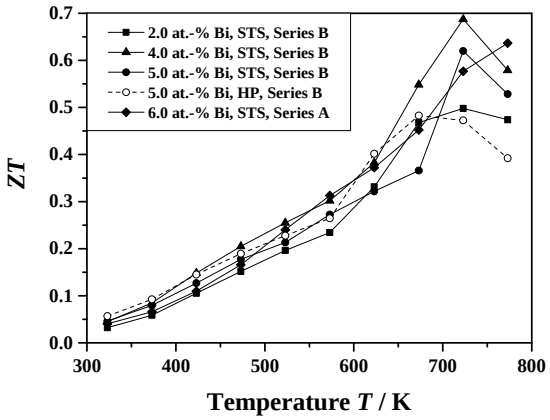

Fig. 12. *ZT* value of bismuth-substituted lead telluride samples (calculated using the thermal conductivity of the first temperature cycle; uncertainty: 20%).

B. Structural properties

Powder X-ray diffraction

Lead telluride crystallizes in the rock salt structure type (space group No. 225, $Fm\bar{3}m$, Altaite).[21,31] For the compound BiTe two different crystal structures are known, a cubic one with the same space group as lead telluride[21,32] and a hexagonal modification (space group No. 164, $P\bar{3}m1$, Tsumoite)[33].

In the XRD patterns of several bismuth-substituted samples which were reground after short term sintering only reflections of the rock salt structure occur and, macroscopically, no elemental crystalline bismuth or any crystalline bismuth telluride-phase like BiTe, Bi_2Te_3 or Bi_4Te_3 were detected, even for samples with higher nominal amounts of bismuth (Fig. 13).

A sharpening of the reflections after annealing during short term sintering (as well as for hot pressing) was observed (Fig. 13). This effect is caused by a thermodynamically induced ordering of the atoms in the crystal structure, which contains a high degree of disorder and amorphous regions due to the milling process prior to annealing. Application of the Scherrer equation on the XRD pattern of the relaxed nanopowders gives an average crystallite size of about 70 nm, determined by using the most intense (200) reflection.

Referring to literature, the lattice constant of the cubic phases varies between a = 6.459 Å for lead telluride[21,31] and a = 6.47 Å for BiTe[21,32]. For mixed crystals, one would expect a very slight increase in the lattice constant with a higher amount of bismuth according to Vegard's law. Yet, for a content of up to 6 at.-% bismuth, a slight decrease is observed (Fig. 14). Starting at about a = 6.462 Å for 1.5 at.-% bismuth with small variations up to a = 6.463 Å for 4.0 at.-% bismuth and decreasing towards about a = 6.460 Å for 5.5 at.-% bismuth, where it remains to be almost constant for 6.0 at.-% bismuth. The unsteady behavior in the lattice constant can be seen as an indication for defect formation at low bismuth contents in lead telluride. This general trend is in rough agreement with literature on the bulk material with a similar amount of bismuth (Fig. 14, Inset).[15]

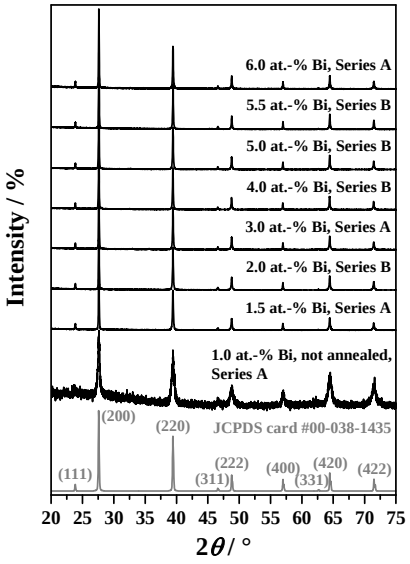

Fig. 13. XRD patterns of reground, short term sintered bismuth-substituted lead telluride nanopowders.

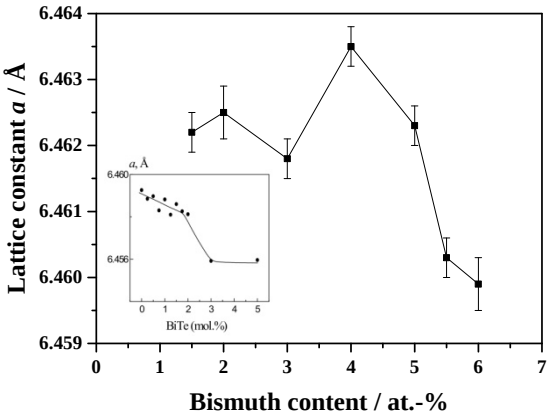

Fig. 14. Lattice parameters of reground, short term sintered bismuth-substituted lead telluride nanopowders. Inset: Lattice parameters of the bulk material; reproduced from Ref. 15.

Raman spectroscopy

Raman spectroscopy is another means of detecting possible precipitations of crystalline phases other than lead telluride. We conducted Raman measurements on some short term sintered samples with different amounts of bismuth.

In Fig. 15 the Raman spectra of samples of both short term sintered series (A + B) are depicted for different bismuth fractions, plus the spectrum of an undoped lead telluride sample as a reference. The positions of the spectra features are compared to literature values (Tab. II).[19]

The surface of the sample investigated was freshly cleaved in order to minimize effects of surface contamination and oxidation which may have arisen during storage of the samples in air atmosphere after synthesis.

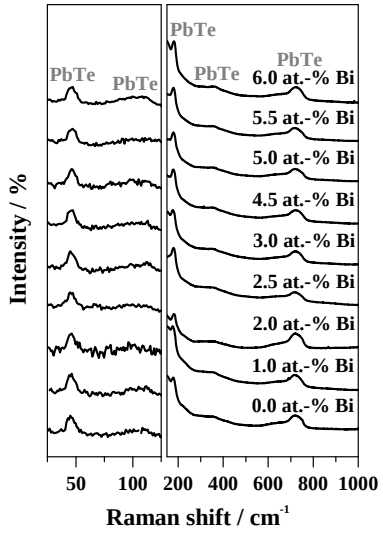

Fig. 15. Raman spectra of short term sintered bismuth-substituted lead telluride samples (Series A + B).

As the average grain size after milling is about 60 nm, we assume that the laser spot (about 300 nm in diameter) samples an ensemble of grains which are agglomerated in the sintering process. The average spectra for the different concentrations of bismuth are shown in Fig. 15. The appearance of all spectra is very similar. The modes in the higher wavenumber region can be assigned to those characteristic for lead telluride. Due to its rock salt structure, lead telluride does not show first-order phonon Raman-scattering. However, second-order Raman scattering is allowed. Furthermore, deviations from the ideality of the crystal structure e. g. due to lattice distortion, defects, non-stoichiometry or plasmonic coupling to the free carriers may induce Raman activity of the first-order processes.[34] The peak at 181 cm^{-1} is usually assigned to a coupled plasmon-phonon mode in the vicinity of an impurity atom in PbTe at high carrier concentrations.[35] It should be noted that the peak at about 139 cm^{-1} is an artefact resulting from the interplay of a rising background of Rayleigh scattered light and the cut-off of the edge filter used in the measurement. The peaks at 362 and 724 cm^{-1} are again lead telluride related and can be assigned to second-order and higher-order multiphonon processes.

Throughout the entire series of spectra three modes can be tentatively assigned in the low wavenumber range. At about 45 (47) cm^{-1} a rather strong mode is seen which is likely to originate from a transversal optical (TO) phonon of lead telluride which becomes Raman-active due to the presence of impurities. The broad peak at about 110 cm^{-1} may consist of contributions due to impurity-induced longitudinal optical (LO) phonon scattering. Tab. II summarizes our findings and gives a comparison with literature data.

It should be noted that all the identified Raman signals are related to lead telluride and do not change on adding bismuth to the material. Furthermore, other Raman signals originating from possible secondary phases such as crystalline bismuth (with corresponding Raman signals at 32, 54, 69, 100, 103 and 109 cm^{-1})[36], bulk Bi_2Te_3 (with four Raman signals at 37, 62, 102,

and 134 cm^{-1} and a further mode for tellurium-rich complexes at about 120 cm^{-1})[37,38], bulk Bi_4Te_3 (with six different Raman signals)[37] or bulk BiTe (with twelve different Raman signals)[37] are not observed. Reliable Raman spectra of the two latter compounds are not available in the literature. In case of such a secondary phase a large number of additional Raman signals not assignable to lead telluride and scaling with bismuth content should occur in the spectra which is also not observed. A scenario in accordance with the Raman results is that bismuth is incorporated into the lead telluride as suggested by the thermoelectric properties and bismuth-rich grain boundaries are formed between the bismuth-doped lead telluride grains. At low bismuth contents a shift of Raman features of lead telluride does not need to arise.

Bismuth does not contribute to any local mode of the lead telluride lattice, thereby not being fully inserted in the surrounding crystal structure of lead telluride, but preferably forming local small bismuth-rich regions, such as 'nanodots' and clusters (probably amorphous), existing next to the matrix.[27] This interpretation is consistent with the XRD data and the discontinuous trend in the lattice parameters, respectively. Thus, nanostructures cannot be detected via XRD or Raman spectroscopy in this particular system, however, the formation of microscopic secondary crystalline phases can be excluded this way.

Table II. Identification of the observed Raman modes of short term sintered bismuth-substituted lead telluride samples and comparison with literature values.

Peak position / cm^{-1}	Mode / description	Literature peak position / cm^{-1}
47	Raman inactive TO mode	45[39], 48[40], 53[34]
110	Forbidden LO phonons / local phonon modes in the vicinity of an impurity atom	104[34], 110[39], 113[40,41], 114[42], 117[19,43,44], 119[35], 121[45]
181	Coupled plasmon-phonon mode / local phonon modes in the vicinity of an impurity atom	181[19,46], 183[35]
362	Second-order Raman scattering	342[19,46,47]
724	Higher-order multi-phonon Raman scattering	724[19,43,46]

Transmission electron microscopy

Exemplarily, TEM investigations of the mechanically alloyed powders show the presence of lenticular nanoparticles with dimensions of about 40 nm to 60 nm with a tendency to agglomerate towards formations of several hundred nanometers (Fig. 16). This is in agreement with the calculations of the crystallite size using the Scherrer equation.

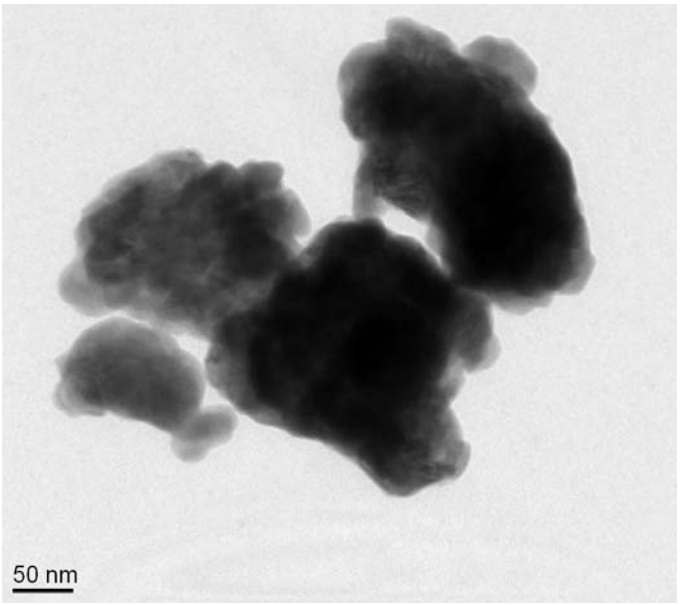

Fig. 16. TEM image of a 6.0 at.-% bismuth-substituted lead telluride nanopowder (Series B).

EDX point analyses with spot sizes between 5.6 and 13.0 nm revealed an inhomogeneous distribution of bismuth in the lead telluride matrix on the nanoscale. A lower average bismuth

content than the nominal addition was found (2.4 at.-% bismuth for a 3.0 at.-% bismuth-substituted sample and 3.6 at.-% bismuth for a 6.0 at.-% bismuth-substituted sample). In the first case, the spot values fluctuate between 2.0 at.-% and 3.0 at.-% bismuth, and between 2.1 at.-% and 4.7 at.-% bismuth in the latter one. One reason for this could be melting of this component at the impact of the milling balls due to its – compared to the other elements – relatively low melting point and a subsequent local precipitation and accumulation, especially at the grain boundaries.

Another option which may explain an inhomogeneous distribution of bismuth is the formation of bismuth-rich clusters in structures close to the building blocks of complex Bi-Te[48] or PbTe-Bi_2Te_3[49] compounds. The infinitely adaptive series $(Bi_2)_m(Bi_2Te_3)_n$[48] comprises a number of phases composed of five-layer lamellae of bismuth telluride and double layers of Bi_2 part of which are of a stoichiometry close to the Bi:Te = 1:1 ratio which may facilitate precipitation in our system $(PbTe)_{1-x}(BiTe)_x$. Alternatively, PbTe-Bi_2Te_3 stoichiometries could form simultaneously to bismuth-rich Bi-Te phases.

However, we do not see any crystalline phases of this type, neither by XRD nor by Raman spectroscopy. Hence, none of such phases has agglomerated to crystallites large enough to be detected. At least, the knowledge of the named complex phases tells us that various configurations among those elements are probable to form in the composition range present in our samples. Such clusters would bind bismuth preventing it to distribute uniformly in the lead telluride matrix. Furthermore, we cannot exclude that the variety of possible phases may undergo transformations when temperature is changing without the need for diffusion on a larger scale to reach a concentration balance. Such transformations might affect thermal and electrical conduction as the Bi-Te phases are highly conductive and might be a reason for the unusual temperature characteristics of electrical and thermal conductivity observed here.

It should be noted that EDX point analysis for structurally inhomogeneous samples is in general not the best choice. An overlapping of the K lines of lead and bismuth which affects the quantification of those elements as seen above cannot be fully excluded. It explains the underestimation of the bismuth content that was found experimentally compared to the nominal weight.

Conclusions

The nanostructured system $Pb_{1-x}Bi_xTe$ prepared by mechanical alloying was studied in the range of $x \leq 0.06$ with regard to its structural and thermoelectric properties. The occurrence of mobility effects, generated by the stoichiometric amounts of bismuth for the substitution of lead (if assumed most likely Bi^{3+} being incorporated to substitute Pb^{2+}) in the lead telluride matrix, was discussed and a comparison with the related system $Bi_x(PbTe)$ was given.

Structural analyses via XRD, Raman spectroscopy and TEM including EDX indicate an inhomogeneous distribution of bismuth and small regions on the nanograin boundaries which are rich in (most likely amorphous) bismuth. Thermal conductivity measurements indicate that those nanostructures precipitate during the first heating of the compacted samples. This inhomogeneous distribution of bismuth could be caused by partial melting during milling and could lead to a preferred

pathway for the charge carrier transport above a critical bismuth content of about 3 at.-%.

Thermoelectric measurements including Hall measurements revealed unsteady changes in the carrier concentration and mobility with varying bismuth concentration which can be attributed to band structure changes of the bismuth-doped lead telluride in combination with the formation of bismuth-rich grain boundary regions. An increase in the amount of bismuth above around 3 at.-% causes a steep rise in the carrier concentration and mobility leading to a notably higher electrical conductivity, especially at low temperatures – much higher than it can be solely expected for a typical doping effect and lower than it would be the case for a possible percolation scenario.

Two different measurement techniques, one for low temperature and one for high temperature measurements, were found to be in good agreement for the electrical conductivity measurement and very good agreement for the determination of the Seebeck coefficient. Furthermore, two independently prepared batches of samples show similar properties. Both points confirm the validity and reproducibility of the presented results.

The rarely used short term sintering technique offers an alternative to the well established process of spark plasma sintering, but the sintering parameters need to be adjusted appropriately for yielding reproducible and highly dense samples. Conventional hot pressing offers an interesting alternative to current-assisted sintering techniques as the corresponding samples yield transport properties comparable to their short term sintered counterparts.

Acknowledgements

This work was financed by the German Research Foundation (DFG) in the priority program SPP 1386 ('Nanostructured Thermoelectrics'). The authors would like to thank Jan Peilstoecker (Institute for Inorganic and Analytical Chemistry, Justus-Liebig-University) for low temperature Seebeck coefficient measurements.

References

1 G. J. Snyder, and E. S. Toberer, *Nat. Mater.* 7, 105 (2008).

2 L. D. Borisova, and S. K. Dimitrova, *Phys. Status Solidi A* 61, K25 (1980).

3 Y.-Z. Pei, A. LaLonde, S. Iwanaga, and G. J. Snyder, *Energy Environ. Sci.* 4, 2085 (2011).

4 J. P. Heremans, V. Jovovic, E. S. Toberer, A. Saramat, K. Kurosaki, A. Charoenphakdee, S. Yamanaka, and G. J. Snyder, *Science* 321, 554 (2008).

5 B. Yu, Q. Zhang, H. Wang, X. Wang, H. Wang, D. Wang, H. Wang, G. J. Snyder, G. Chen, and Z.-F. Ren, *J. Appl. Phys.* 108, 016104 (2010).

6 J.-Q. Li, S.-P. Li, Q.-B. Wang, L. Wang, F.-S. Liu, and W.-Q. Ao, *J. Electron. Mater.* 40, 2063 (2011).

7 L. Ruan, J. Luo, H. Zhu, H. Zhao, and J. Liang, *J. Electron. Mater.* 44, 3556 (2015).

8 L. D. Borisova, and S. K. Dimitrova, *Bulg. J. Phys.* 4, 414 (1977).

9 L. D. Borisova, *Phys. Status Solidi A* 53, K19 (1979).

10 M. Schenk, H. Berger, C. Kleint, N. S. Golovanova, O. I. Tananaeva, and V. P. Zlomanov, *Phys. Status Solidi A* 91, K35 (1985).

11 L. D. Borisova, *Bulg. J. Phys.* 13, 43 (1986).

12 T. A. Christakudi, G. C. Christakudis, and L. D. Borisova, *Phys. Status Solidi A* 114, K201 (1989).

13 E. I. Rogacheva, and S. G. Luibchenko, *J. Thermoelectr.* 3, 24 (2005).

14 E. I. Rogacheva, S. G. Luibchenko, and O. S. Vodorez, *Funct. Mater.* 13, 571 (2006).

15 T. V. Tavrina, E. I. Rogacheva, and V. I. Pinegin, *Mold. J. Phys. Sci.* 4, 430 (2005).

16 J. He, J. R. Sootsman, S. N. Girard, J.-C. Zheng, J. Wen, Y. Zhu, M. G. Kanatzidis, and V. P. Dravid, *J. Am. Chem. Soc.* 132, 8669 (2010).

17 A. Popescu, A. Datta, G. S. Nolas, and L. M. Woods, *J. Appl. Phys.* 109, 103709 (2011).

18 J. R. Sootsman, R. J. Pcionek, H. Kong, C. Uher, and M. G. Kanatzidis, *Chem. Mater.* 18, 4993 (2006).

19 A. Bali, E. Royanian, E. Bauer, P. Rogl, and R. C. Mallik, *J. Appl. Phys.* 113, 123707 (2013).

20 O. Falkenbach, D. Hartung, P. J. Klar, G. Koch, and S. Schlecht, *J. Electron. Mater.* 43, 1674 (2014).

21 D. R. Lide, *Handbook of Chemistry and Physics* 77th Ed., CRC Press, Boca Raton (1996).

22 A. S. Pashinkin, M. S. Mikhailova, A. S. Malkova, and V. A. Fedorov, *Inorg. Mater.* 45, 1226 (2009).

23 G. Homm, M. Piechotka, A. Kronenberger, A. Laufer, F. Gather, D. Hartung, C. Heiliger, B. K. Meyer, P. J. Klar, S. O. Steinmueller, and J. Janek, *J. Electron. Mater.* 39, 1504 (2010).

24 A. A. El-Sharkawy, A. M. Abou El-Azm, M. I. Kenawy, A. S. Hillal, and H. M. Abu-Basha, *Int. J. Thermophys.* 4, 261 (1983).

25 E. D. Case, *J. Electron. Mater.* 41, 1811 (2012).

26 Y.-Z. Pei, X.-Y. Shi, A. LaLonde, H. Wang, L.-D. Chen, and G. J. Snyder, *Nature* 473, 66 (2011).

27 K. Hoang, S. D. Mahanti, and M. G. Kanatzidis, *Phys. Rev. B* 81, 115106 (2010).

28 D. L. Partin, C. M. Thrush, S. J. Simko, and S. W. Gaarenstroom, *J. Appl. Phys.* 66, 6115 (1989).

29 A. Y. Ueta, G. Springholz, F. Schinagl, G. Marschner, and G. Bauer, *Thin Solid Films* 306, 320 (1997).

30 W. Tamura, A. Yasuda, K. Suto, O. Itoh, and J.-I. Nishizawa, *J. Electron. Mater.* 32, 39 (2003); W. Tamura, A. Yasuda, K. Suto, M. Hosokawa, O. Itoh, and J.-I. Nishizawa, *J. Electron. Mater.* 32, 1079 (2003).

31 (a) Crystallographic data sheet PbTe, *JCPDS card,* No. 00-038-1435. (b) C. A. Peck, and R. B. Ruokolainen, *Powder Diffr.* 2, 230 (1987).

32 (a) Crystallographic data sheet BiTe, *JCPDS card,* No. 00-015-0820. (b) *Natl. Bur. Stand. (U. S.) Monogr. 25* 4, 50 (1965).

33 (a) Crystallographic data sheet BiTe, *JCPDS card,* No. 01-083-1749. (b) H. Shimazaki, and T. Ozawa, *Am. Mineral.* 63, 1162 (1978).

34 J. Trajić, A. Golubović, M. Romčević, N. Romčević, S. Nikolić, and V. N. Nikiforov, *J. Serb. Chem. Soc.* 72, 55 (2007).

35 H.-Z. Wu, C.-F. Cao, J.-X. Si, T.-N. Xu, H.-J. Zhang, H.-F. Wu, J. Chen, W.-Z. Shen, and N. Dai, *J. Appl. Phys.* 101, 103505 (2007).

36 G.-Q. Huang, and J. Yang, *J. Phys.: Condens. Matter* 25, 175004 (2013).

37 V. Russo, A. Bailini, M. Zamboni, M. Passoni, C. Conti, C. S. Casari, A. L. Bassi, and C. E. Bottani, *J. Raman Spectroc.* 39, 205 (2008).

38 (a) W. Richter, H. Koehler, and C. R. Becker, *Phys. Status Solidi B* 84, 619 (1977). (b) W. Kullmann, J. Geurts, W. Richter, N.

Lehner, H. Rauh, U. Steigenberger, G. Eichhorn, and R. Geick, *Phys. Status Solidi B* 125, 131 (1984). (c) V. Chis, I. Y. Sklyadneva, K. A. Kokh, V. A. Volodin, O. E. Tereshchenko, and E. V. Chulkov, *Phys. Rev. B* 86, 174304 (2012). (d) G. D. Keskar, R. Polida, L.-H. Zhang, A. M. Rao, and L. D. Pfefferle, *J. Phys. Chem. C* 117, 9446 (2013). (e) A. F. Zurhelle, V. L. Deringer, R. P. Stoffel, and R. Dronskowski, *J. Phys.: Condens. Matter* 28, 115401 (2016).

39 S. Ves, Y. A. Pusep, K. Syassen, and M. Cardona, *Solid State Commun.* 70, 257 (1989).

40 H. W. Leite Alves, A. R. R. Neto, L. M. R. Scolfaro, T. H. Myers, and P. D. Borges, *Phys. Rev. B* 87, 115204 (2013).

41 S. V. Ovsyannikov, Y. S. Ponosov, V. V. Shchennikov, and V. E. Mogilenskikh, *Phys. Status Solidi C* 1, 3110 (2004).

42 W. Cochran, R. A. Cowley, G. Dolling, and M. M. Elcombe, *Proc. R. Soc. London, Ser. A* 293, 433 (1966).

43 M. Romčević, N. Romčević, D. R. Khokhlov, and I. I. Ivanchik, *J. Phys.: Condens. Matter* 12, 8737 (2000).

44 F.-J. Kong, Y.-H. Liu, B.-L. Wang, Y.-Z. Wang, and L.-L. Wang, *Comput. Mater. Sci.* 56, 18 (2012).

45 T.-Y. Shu, P.-Q. Lu, B.-P. Zhang, M. Wang, L. Chen, X.-L. Fu, G.-Y. Xu, and H.-Z. Wu, *J. Cryst. Growth* 420, 17 (2015).

46 N. Romčević, J. Trajić, B. Hadžić, M. Romčević, D. Stojanović, Z. Lazarević,T. A. Kuznetsova, D. R. Khokhlov, R. Rudolf, and I. Anžel, *Acta Phys. Pol. A* 116, 91 (2009).

47 A. H. Romero, M. Cardona, R. K. Kremer, R. Lauck, G. Siegle, J. Serrano, and X. C. Gonze, *Phys. Rev. B* 78, 224302 (2008).

48 J. W. G. Bos, H. W. Zandbergen, M.-H. Lee, N. P. Ong, and R. J. Cava, *Phys. Rev. B* 75, 195203 (2007).

49 L. E. Shelimova, O. G. Karpinskii, T. E. Svechnikova, E. S. Avilov, M. A. Kretova, and V. S. Zemskov, *Inorg. Mater.* 40, 1264 (2004).

Figure captions:

Fig. 1. Thermal conductivity of bismuth-substituted lead telluride samples (first temperature cycle).

Fig. 2. Electrical conductivity of short term sintered bismuth-substituted lead telluride samples (Series A).

Fig. 3. Electrical conductivity of short term sintered bismuth-substituted lead telluride samples (Series B).

Fig. 4. Electrical conductivity of hot pressed bismuth-substituted lead telluride samples (Series B).

Fig. 5. Electrical conductivity of bismuth-substituted lead telluride samples at 223 K and 623 K, respectively.

Fig. 6. Carrier concentration of bismuth-substituted lead telluride samples at 280 K.

Fig. 7. Carrier mobility of bismuth-substituted lead telluride samples at 280 K.

Fig. 8. Seebeck coefficient of short term sintered bismuth-substituted lead telluride samples (Series A).

Fig. 9. Seebeck coefficient of short term sintered bismuth-substituted lead telluride samples (Series B).

Fig. 10. Seebeck coefficient of hot pressed bismuth-substituted lead telluride samples (Series B).

Fig. 11. Seebeck coefficient of bismuth-substituted lead telluride samples at 223 K and 623 K, respectively.

Fig. 12. *ZT* value of bismuth-substituted lead telluride samples (calculated using the thermal conductivity of the first temperature cycle).

Fig. 13. XRD patterns of reground, short term sintered bismuth-substituted lead telluride nanopowders.

Fig. 14. Lattice parameters of reground, short term sintered bismuth-substituted lead telluride nanopowders. Inset: Lattice parameters of the bulk material; reproduced from Ref. 15.

Fig. 15. Raman spectra of short term sintered bismuth-substituted lead telluride samples (Series A + B).

Fig. 16. TEM image of a 6.0 at.-% bismuth-substituted lead telluride nanopowder (Series B).